

## MAPPING GALAXY EVOLUTION BY ANALYZING MORPHOLOGY IN SIMBA SIMULATIONS & HUBBLE EXTREME DEEP FIELD OBSERVATIONS

DANIELLA MORRONE<sup>1</sup> AND ADVISORS: DR. LAMIYA MOWLA<sup>2</sup> & DR. KARTHEIK IYER<sup>2</sup>

### 1. INTRODUCTION

Galaxy morphology and evolution are two highly understudied fields in astronomy research; even more-so, how the two correspond. Specifically, how galaxy morphology - the study of the shape, size, composition of galaxies - relates to and plays a role in galaxy evolution - the study of how galaxies change and develop over their lifetime - is a notably underrepresented field of research.

Galaxy evolution presents the composition of galaxies in a new perspective, through mergers, quenching, star bursts and other physical phenomena that occur in and between galaxies. These events introduce unique characteristics in galaxy mass and light distributions that, when analyzed, reveal important features of galaxy composition and history. Light profiles as well as features of galaxy morphology, including mass, star formation rate and more, are tracers of evolutionary events in galaxies' lives. Light emitted from galaxies at various wavelengths highlight key features of galaxy composition: old stars emit redder light while young stars emit bluer light; galactic dust causes reddening of emitted light. These features allow for predictions of the composition of galaxies. However, light is a biased tracer of the true composition, providing an estimate of the mass in the galaxy. Mass however is the true determinant of the composition of a galaxy and allows for more relevant studies of characteristic moments in galaxy evolution.

However, recent observational studies on galaxies review evolution solely in terms of light profiles or physical properties (such as stellar mass, star formation rate (SFR), etc.), without delving into how the two compare (examples of these studies: Kurczynski et al. 2016; Bouwens et al. 2017; Huang et al. 2017; Holwerda et al. 2020). This lack of investigation into physical property maps in conjunction with light profiles is due to the difficulty of obtaining such information. Only light can be observed from a galaxy and thus all predictions of mass, star formation rate, and other properties are based solely off those light profiles. Consequently, most observational studies review morphology using a subset of galaxy components. Conversely, numerous studies, including Genel et al. (2014); Duffy et al. (2017); Côté et al. (2018); Ma (2018); de Graaff et al. (2021); Robson & Davé (2021), investigate structures and physical properties of simulated galaxies and evolutionary implications of such features. Further, studies to compare observed and simulated galaxy measurements, such as Bouwens et al. (2017); Huang et al. (2017); Adams et al. (2021); Fontanot et al. (2021); Zheng et al. (2021), investigate light-weighted morphology without comparing to phys-

ical property maps, or vice-versa. These above points present a gap in the current studies on galaxy morphology and evolution: the use of light-weighted morphology in conjunction with physical property maps to study galaxy evolution in simulations and real observation.

Moreover, simulations present the opportunity for mock observations to be used. However, many studies that use mock observations only investigate predictions of data from upcoming releases and telescopes (for example, James Webb Space Telescope (JWST)), and anticipate their results; examples of such studies are Endsley et al. (2020); Hainline et al. (2020); Kauffmann et al. (2020). Thus, another gap is present in this field of research: comparing mock observations, alongside simulations, to real galaxy observations as a means to gauge the accuracy of measurements and explore any discrepancies between what is expected and what is truly occurring.

Studies on galaxy morphology and evolution are constrained to analyzing light profiles and their corresponding physical property maps. Extending studies comparing these light- and mass-weighted morphology on observations to simulations and mock observations allows for an opportunity to investigate the accuracy of the predicted properties (simulations) of galaxies compared to measurements of true properties (observations), allowing for a more in-depth analysis of any trends between light profiles and physical properties. However, the aforementioned constraints have limited the studies done on galaxy morphology and evolution, thus presenting two current gaps in this field of research: (i) the comparison of observations and simulations in analyzing both the light- and mass-weighted morphology of galaxies, and (ii) the use of mock observations in conjunction with real observations and simulations to probe the accuracy of measurements and the simulations themselves. In this report, we investigate these two gaps via light-morphology - a biased tracer of galaxy composition - and mass-morphology - an unbiased tracer - of observed, mock and simulated galaxies, as a means to map out galaxy evolution.

### 2. METHODS

To explore galaxy morphology and evolution, and the aforementioned gaps in this field, we investigate relationships between stellar mass ( $M_*$ ), light and specific star formation rate (sSFR) in simulated, mock and real galaxies for redshifts  $0.25 < z < 6$  and  $M_* \geq 10^9 M_\odot$ . Specifically, we study this galaxy population in the Hubble eXtreme Deep Field (Illingworth et al. 2013) and the SIMBA suite of cosmological simulations (Davé et al. 2019).

#### 2.1. *Hubble eXtreme Deep Field (XDF)*

The Hubble eXtreme Deep Field (XDF), seen in Figure 2, is used in this study as the observed galaxy population. The XDF combines 10 years of Hubble

<sup>1</sup> University of Toronto

<sup>2</sup> Dunlap Institute for Astronomy & Astrophysics

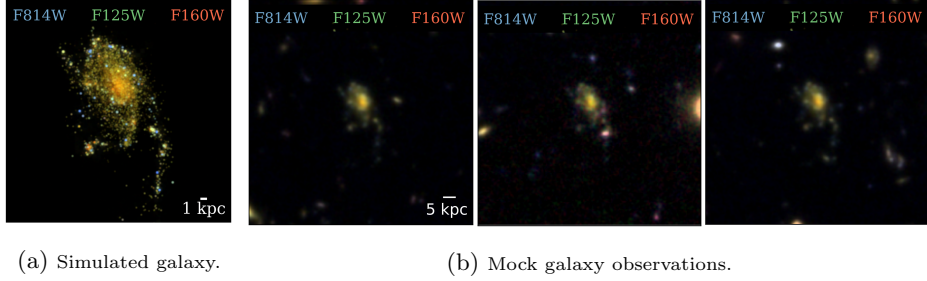


FIG. 1.—: (a) Simulated and (b) mock galaxy at  $z=2$  through 3 HST filters: F814W, F125W, F160W. Credit: Dr. Lamiya Mowla.

Space Telescope (HST) data from the HST Advanced Camera for Surveys (ACS) and the Wide-Field Camera 3 Infra-Red (WFC3/IR) instruments (Illingworth et al. 2013). Including data from 9 HST filters (F435W at  $0.435\mu m$ , F606W at  $0.606\mu m$ , F775W at  $0.775\mu m$ , F814W at  $0.814\mu m$ , F850LP at  $0.850\mu m$ , F105W at  $1.05\mu m$ , F125W at  $1.25\mu m$ , F140W at  $1.40\mu m$ , F160W at  $1.6\mu m$ ), the XDF spans a field of  $10.8 \text{ arcmin}^2$ , a total exposure time of 22.5 days, and at a size of 5250 pixels by 5250 (Illingworth et al. 2013). Note that the F850LP filter was not used for this study and the point-spread function (PSF)-convolved images of the remaining 8 filters, from Sorba & Sawicki (2018), were used. This observation presents the deepest sky image in the optical/near-IR to date, a combined depth of 31.2 AB mag ( $5\sigma$ ) (Illingworth et al. 2013). From this field, the mass and star formation maps of the galaxy population were found using `dense_basis` (Iyer et al. 2019). This package uses spectral energy distributions (SED) to fit each pixel on the image individually, converting the galaxy light into physical properties.

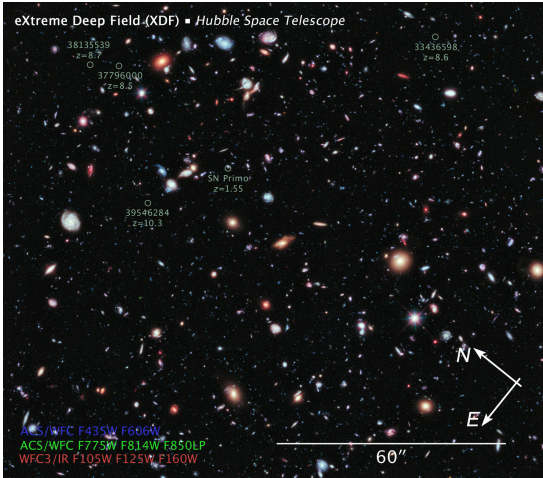


FIG. 2.—: The Hubble eXtreme Deep Field compass image. This image is a composite of separate exposures acquired by the ACS and WFC3/IR instruments. Several filters were used to sample various wavelengths. Credit: NASA, ESA, G. Illingworth, D. Magee, and P. Oesch (University of California, Santa Cruz), R. Bouwens (Leiden University), and the HUDF09 Team.

## 2.2. SIMBA Simulations

The SIMBA suite of simulations was used for the simulated and mock observed galaxy populations, providing both their light-weighted morphology and physical property distributions. The SIMBA suite presents cosmological galaxy formation simulations, run with meshless finite mass hydrodynamics (Davé et al. 2019). As the next generation of the MUFASA simulations, SIMBA has im-

proved dust accretion and attenuation processes, introduces the torque-limited accretion model of black hole growth (Anglés-Alcázar et al. 2017), and more. Thus, the SIMBA suite presents new additions of important physical processes to our galaxy population. Used alongside these simulated galaxies, mock observations of this population were generated by applying the `POWDERDAY` radiative transfer package (Narayanan et al. 2021) onto simulated galaxies to produce mock observations as seen through various instruments in a specified field. Figure 1 shows the same galaxy as 1a: a simulation, and 1b: mock observations.

### 2.3. Data Reduction (Cuts) & Measurement Pipeline

The quantity of galaxies in both our original populations were too abundant and too broad for this study and needed to be cut down and reduced before proceeding in this research. The XDF itself contains 9156 galaxies; however, not all these galaxies were used for this work. For some sources at higher redshifts, the signal-to-noise was too low or did not encompass enough pixels for accurate fitting. Thus, a cut was placed on the number of pixels of an individual galaxy:  $N_{pix} \geq 100$ . Further, the galaxy population was chosen to have  $0.25 < z < 6$  and  $M_* \geq 10^8 M_\odot$ . With a total of 853 XDF galaxies meeting these cuts, the same restrictions were placed on the SIMBA suite to yield a similar galaxy population.

The measurements obtained from the stellar mass and light profiles of the galaxy populations were half-mass and half-light radii; that is, the radii of circular apertures containing half the flux of an image: mass or light, respectively. Such measurements of the galaxy populations were acquired using a pipeline which was developed in May-August 2021 and continually developed through the duration of this project. The pipeline consists of three different approaches to obtaining the measurements: aperture fitting via `astropy` Python package (Astropy Collaboration et al. 2013, 2018) for the simulated galaxies; Sérsic fitting via `statmorph` Python package (Rodríguez-Gómez et al. 2019), and multi-Gaussian ( $N=4$ ), Bayesian fitting via `imcascode` Python package (Miller & van Dokkum 2021) for the mock and real observed galaxy populations.

Applying the pipeline, we were able to measure the half-light and half-mass radii for our simulated, observed and mock galaxy populations. We then investigated how these size measurements evolve as functions of stellar mass, sSFR and redshift, and how the size evolution of each galaxy population compare to each other. For this report, only the measurements from the simulated, aperture fit galaxies and the observed galaxies fit through `imcascode` will be presented, with an emphasis on the latter, as that was the focus of this project.

### 3. RESULTS AND DISCUSSION

#### 3.1. Observations: XDF

The real observed galaxy population used in this work was from the XDF. Containing 9156 galaxies, this population was cut down to 853 using the cuts on redshift, stellar mass and pixel size on the field. From here, the measurements of half-mass ( $r_{\text{mass}}$ ) and half-light ( $r_{\text{light}}$ ) radii found using the `imcasclade` Python package. This package outputted measurements on 20%, 50%, 80%, 90% the flux of the given image; we used the 50% measurements. However, several fits yielded inconclusive results; if the fitting software produced an error, the measurement was recorded as 0; if the fitting software could not fit the given galaxy, a default value was output:  $r_{\text{err}} = 5.27884301349054$  pixels. After filtering out these inconclusive measurements, significantly fewer galaxies were left to analyze. Table 1 shows the resulting number of measurements to analyze.

The measurements from this work were compared against similar studies by Mowla et al. (2019) and Suess et al. (2019), seen in Figures 3 and 4, respectively. Mowla et al. (2019) discusses the size-mass distribution of galaxy populations in the COSMOS-DASH survey with  $\log(M_*/M_\odot) > 11.3$  and  $0.1 < z < 3$ . We have compared this to our work on the XDF, extending the fits to lower stellar masses, to higher redshifts, and to light profiles. These parameterized fits follow Equation 1.

$$\left(\frac{r_{50}}{\text{kpc}}\right) = A \left(\frac{M_*}{5 \times 10^{10} M_\odot}\right)^\alpha \quad (1)$$

where  $r_{50}$  is the effective radius in kiloparsecs; this value is the half-mass and -light radii in our work and just the half-mass radius in Mowla et al. (2019). The parameters  $A$  and  $\alpha$  are fit to our galaxy population, as seen in Table 2 and the black curves in Figure 3. Compared against the fit from Mowla et al. (2019) at the highest redshift ( $z = 2.75$ :  $A = 0.50 \pm 0.02$ ,  $\alpha = 0.13 \pm 0.03$ ), our fits tend to be as expected: in Figure 3, our fits, including redshifts  $0.25 \leq z \leq 6$ , are lower than those from Mowla et al. (2019), which trend downwards with increasing redshift. As expected, when reviewing the distribution of the  $r_{50}$  values at  $z \geq 2.75$ , most reside below 2.5 kpc at all 8 filters. This is agreeable with the expected downward trend of the fits in Mowla et al. (2019). Further, the fits from both the literature and this work are consistent at lower stellar masses. However, upon reviewing the residuals for the F160W measurements (see Figure 5), all fits, including from Mowla et al. (2019) and from this work, produced very large residuals. Any residuals  $> 5$  were considered outliers; however, the spread was extensive, with standard deviations of  $\sigma \sim 2$  for residuals on all fits.

Suess et al. (2019) analyzes the size-mass distribution and mass-to-light relations of galaxy populations in the CANDELS field survey with  $9 \leq \log(M_*/M_\odot) \leq 11.5$  and  $1.0 \leq z \leq 2.5$ . Comparing this to our work and extending the fits to  $\log(M_*/M_\odot) \leq 12$  and  $0.25 \leq z \leq 6$ , our measurements were fit following Equation 2.

$$\log\left(\frac{r_{\text{mass}}}{r_{\text{light}}}\right) = s \log\left(\frac{M_*}{M_\odot} - 10\right) + b \quad (2)$$

where  $r_{\text{mass}}/r_{\text{light}}$  is the half-mass-to-light ratio. Our fits differ from the anticipated fits in Suess et al. (2019), notably when observed at longer wavelengths. Using

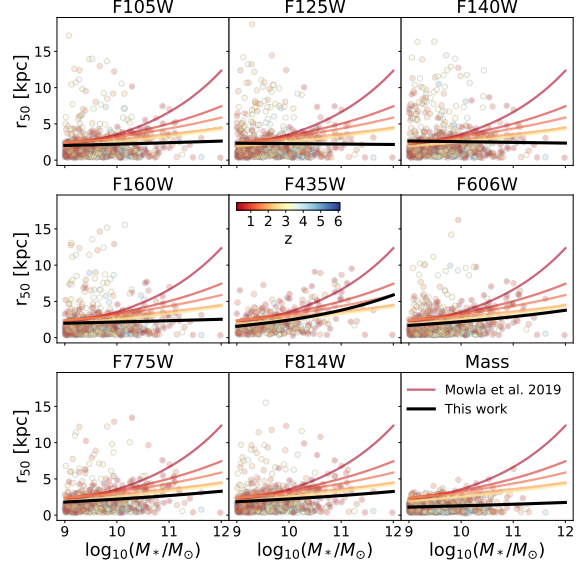


FIG. 3.—: Size distribution of galaxies in the XDF at 8 HST filters and through their mass maps. Parameterized fits, from Equation 1, are plotted as the black line on all 9 subplots, compared against results from Mowla et al. (2019) for the COSMOS-DASH survey at 6 redshift bands ( $z=0.25, 0.75, 1.25, 1.75, 2.25, 2.75$ ), plotted as 6 lines on each subplot, coloured by redshift.

the F160W measurements, we analyzed the residuals on these fits for  $1 \leq z \leq 2.5$  and noticed that the scatter was very small, with most residuals within  $0 \pm 1$  and standard deviations of  $\sigma \sim 0.37$  on each fit. While the scatter is small, indicating the fits hugged the data closely, there is still a slight upward trend towards zero for the three fits from Suess et al. (2019).

We now narrow our focus to a subset of the galaxy population:  $\log(M_*/M_\odot) \geq 10$  and  $0.5 \leq z \leq 3$ . In Figure 6, the half-mass-to-light relation is plotted as a function of restframe wavelength for 98 galaxies within these parameters. The distribution of these measurements spans

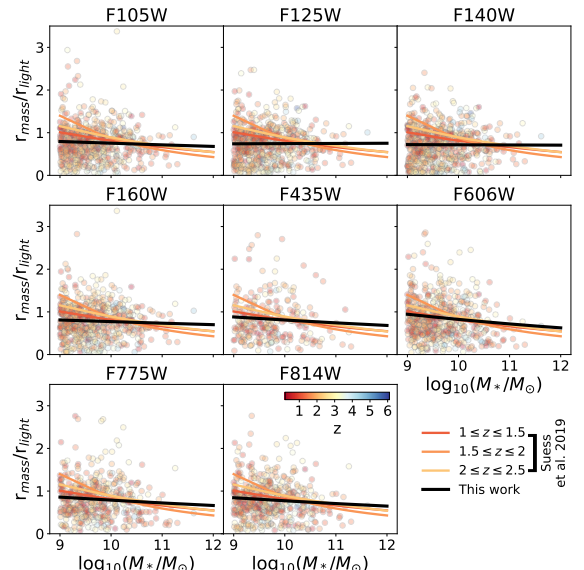


FIG. 4.—: Half-mass-to-light ratio distribution of galaxies in the XDF at 8 HST filters. The parameterized fits, from Equation 2, of these measurements are plotted as the black line on all 8 subplots, compared against results from Suess et al. (2019) of the CANDELS fields at 3 redshift ranges ( $1 \leq z \leq 1.5$ ,  $1.5 \leq z \leq 2$ ,  $2 \leq z \leq 2.5$ ), plotted as 3 lines on each subplot, coloured by redshift.

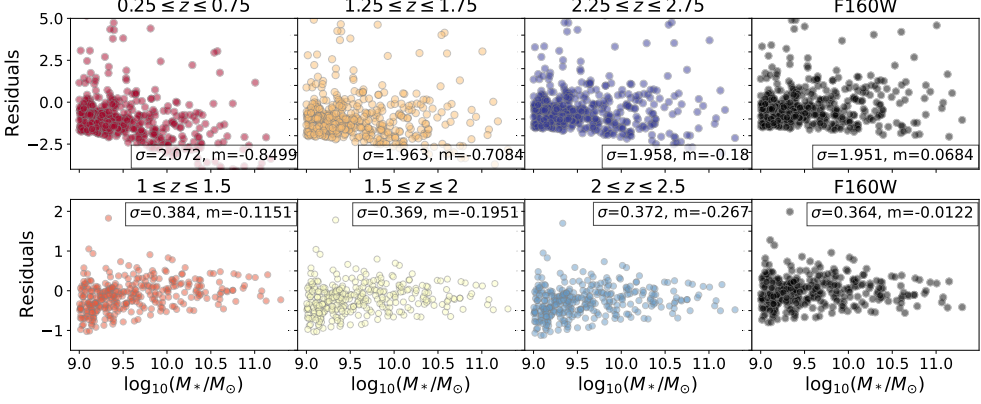


FIG. 5.—: Residuals of the parameterized fits on the F160W measurements. The standard deviation ( $\sigma$ ) and mean (m) on the residuals for each fit are recorded on each subplot. Top row: Equation 1 fitting on  $0.25 \leq z \leq 2.75$  XDF galaxies, with the left 3 subplots using the fit from Mowla et al. (2019) and far right subplot using the fit found in this work. Similarly, bottom row: Equation 2 fitting for  $1 \leq z \leq 2.5$ , with the left 3 subplots from Suess et al. (2019) and far right subplot from this work.

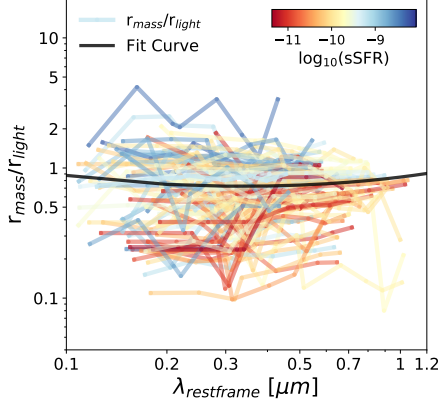


FIG. 6.—: The half-mass ( $r_{\text{mass}}$ ) to half-light ( $r_{\text{light}}$ ) ratio plotted as a function of restframe wavelength for 98 XDF galaxies within the galaxy population of  $M_* \geq 10^{10} M_\odot$ ,  $0.5 \leq z \leq 3$ , with a black curve of best fit over the measurements.

quite a large range. However, a trend can be noticed: more star forming galaxies reside on the lower end of the mass-to-light ratio, meaning the half-light radii are larger; less star forming galaxies have larger mass-to-light ratios and thus have larger half-mass radii. This trend opposes what is found in the simulations and in current literature; we discuss this in the next section (§3.2).

### 3.2. SIMBA Simulations & Mock Observations

First, we confirmed that our pipeline yields the desired outputs by comparing a simulated galaxy at  $z=2$  to 20 iterations of its mock observation. This comparison, in Figure 7, shows that the measurement pipeline outputted values following very closely the same trend as a function of restframe wavelength for both the simulated and mock

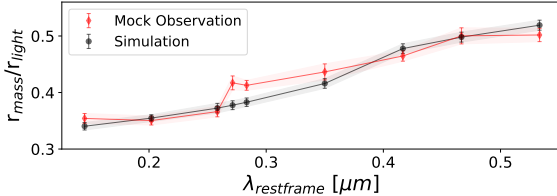


FIG. 7.—: The half-mass-to-light relation for a galaxy at  $z=2$  through simulations and mock observations plotted as a function of restframe wavelength. Measurements from 20 variations of the mock observation were averaged to yield these values.

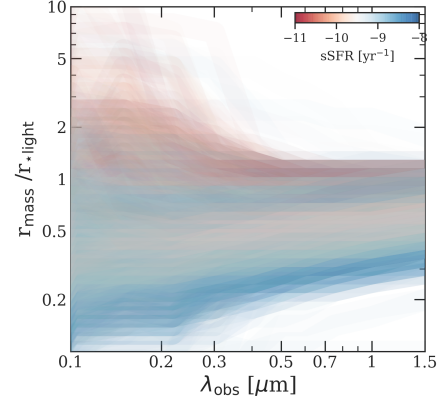


FIG. 8.—: The half-mass ( $r_{\text{mass}}$ ) to half-light ( $r_{\text{light}}$ ) ratio plotted against restframe wavelength for  $\sim 13000$  SIMBA simulated galaxies within the galaxy population of  $M_* \geq 10^{10} M_\odot$ ,  $0.5 \leq z \leq 3$ , with a black curve of best fit over the measurements. Credit: Dr. Lamiya Mowla.

measurements. This proved that the pipeline worked as it was intended.

Similar to the work done in Section 3.1, the mass-to-light relation was analyzed for SIMBA simulated galaxies of  $\log(M_*/M_\odot) \geq 10$  and  $0.5 \leq z \leq 3$ . A reverse trend was noticed in this analysis, as seen in Figure 8, when compared to the observations. This trend in the simulations is consistent with what is found in current literature (see de Graaff et al. (2021)), and more investigation is needed to understand what caused this discrepancy in the observed measurements.

### 4. CONCLUSIONS & FUTURE WORK

The observational research presented in this report agrees with work previously done on size-mass distributions of similar galaxy populations and presents new trends for galaxies at higher redshifts and lower stellar mass. In particular, this work is in agreement on the effective radius fits ( $r_{50}$ ) with those in Mowla et al. (2019), and the half-mass-to-light ratio ( $r_{\text{mass}}/r_{\text{light}}$ ) with those in Suess et al. (2019). However, the measurements posed a unique situation in which the sSFR trends with the size distribution differently in the simulations than the observations. Numerous reasons could be the cause for this. Namely, the observations are specifically chosen to have sizes  $> 100$  pixels on the field and thus disregards any smaller, lower signal-to-noise galaxies which the sim-

Filter	N	$N_0$	$N_r$	Redshifts	log-Stellar Mass	log-sSFR	$r_{50}$
F105W	696	59	98	$0.251 \leq z \leq 5.756$	$9.0005 \leq \log(M_*) \leq 11.9834$	$-11.3689 \leq \log(\text{sSFR}) \leq -8.0641$	$0.2885 \leq r_{50} \leq 15.5065$
F125W	733	31	89	$0.251 \leq z \leq 5.756$	$9.0005 \leq \log(M_*) \leq 11.9834$	$-11.3689 \leq \log(\text{sSFR}) \leq -8.0641$	$0.2885 \leq r_{50} \leq 15.5065$
F140W	735	67	51	$0.251 \leq z \leq 5.756$	$9.0005 \leq \log(M_*) \leq 11.9834$	$-11.3689 \leq \log(\text{sSFR}) \leq -8.0641$	$0.2885 \leq r_{50} \leq 15.5065$
F160W	740	43	70	$0.251 \leq z \leq 5.756$	$9.0005 \leq \log(M_*) \leq 11.9834$	$-11.3689 \leq \log(\text{sSFR}) \leq -8.0641$	$0.2885 \leq r_{50} \leq 15.5065$
F435W	344	45	464	$0.293 \leq z \leq 4.684$	$9.0007 \leq \log(M_*) \leq 11.9834$	$-11.3039 \leq \log(\text{sSFR}) \leq -8.2359$	$0.2885 \leq r_{50} \leq 15.5065$
F606W	665	14	174	$0.251 \leq z \leq 4.712$	$9.0005 \leq \log(M_*) \leq 11.9834$	$-11.3512 \leq \log(\text{sSFR}) \leq -8.0641$	$0.2885 \leq r_{50} \leq 15.5065$
F775W	575	20	258	$0.251 \leq z \leq 4.754$	$9.0005 \leq \log(M_*) \leq 11.9834$	$-11.3512 \leq \log(\text{sSFR}) \leq -8.0641$	$0.2885 \leq r_{50} \leq 15.5065$
F814W	618	36	199	$0.251 \leq z \leq 5.756$	$9.0005 \leq \log(M_*) \leq 11.9834$	$-11.3512 \leq \log(\text{sSFR}) \leq -8.0641$	$0.2885 \leq r_{50} \leq 15.5065$
Mass	724	129	0	$0.249 \leq z \leq 5.756$	$9.0005 \leq \log(M_*) \leq 11.6178$	$-11.3689 \leq \log(\text{sSFR}) \leq -8.0641$	$0.2885 \leq r_{50} \leq 15.5065$

TABLE 1: Properties of the galaxy population subset from the XDF. The filter (or mass, where applicable) is recorded alongside the number of properly fit galaxies (N), the number which received an error ( $N_0$ ) and number which yielded  $r_{err} = 5.27884301349054$  pixels. ( $N_r$ ), all as output from the software. This table includes the ranges of the galaxy redshifts (z), log-stellar mass ( $\log(M_*/M_\odot)$ ), log-specific star formation rate ( $\log(\text{sSFR})$ ), and the measurements of half-light or half-mass, respectively ( $r_{50}$ ).

	F105W	F125W	F140W	F160W	F435W	F606W	F775W	F814W	Mass
Fitting size distribution using Equation 1.									
logA	$0.37 \pm 0.03$	$0.35 \pm 0.03$	$0.39 \pm 0.04$	$0.36 \pm 0.03$	$0.52 \pm 0.02$	$0.42 \pm 0.03$	$0.4 \pm 0.03$	$0.41 \pm 0.03$	$0.16 \pm 0.02$
Fitting mass-to-light size distribution using Equation 2.									
s	$-0.023 \pm 0.021$	$0.003 \pm 0.019$	$-0.003 \pm 0.02$	$-0.021 \pm 0.018$	$-0.037 \pm 0.036$	$-0.06 \pm 0.027$	$-0.038 \pm 0.023$	$-0.038 \pm 0.022$	—
b	$-0.123 \pm 0.012$	$-0.129 \pm 0.012$	$-0.145 \pm 0.012$	$-0.113 \pm 0.011$	$-0.092 \pm 0.021$	$-0.084 \pm 0.016$	$-0.104 \pm 0.013$	$-0.112 \pm 0.013$	—

TABLE 2: Results from the size distribution of galaxies in the XDF at 8 HST filters and through their mass maps, and from the mass-to-light size distribution. The parameterized fits can be seen in Figures 3 and 4, from Equations 1 and 2, respectively.

ulations include. This is an aspect of this work which requires further attention to determine the true cause of this discrepancy.

This report proposes the initial work towards mapping galaxy evolution through mass- and light-weighted morphology by analyzing observational data alongside both simulations and mock observations. The work done on this project can be extended beyond the bounds outlined in this report. Notably, the galaxy population can be broadened to cover larger redshift ranges and lower mass galaxies, with lower signal-to-noise and spanning fewer pixels on the field. These extensions will allow for further mapping of galaxy evolution at the ex-

tremes. Beyond this, the filters at which observations are made can be extended to both shorter and longer wavelengths. With these prospective extensions, a proposed future goal for this work would be to use the measurements on the light- and mass-morphology to analyze key structural differences between galaxies (i.e. mergers, dark matter distribution, etc.), similar to work done in McLure et al. (2013). Further, with the recent launch of the James Webb Space Telescope (JWST) in December 2021, galaxy populations at higher redshifts, lower signal-to-noise, and a larger range of wavelengths will be more accessible and abundant to be studied.

## REFERENCES

- Adams, N. J., Bowler, R. A. A., Jarvis, M. J., Häufner, B., & Lagos, C. D. P. 2021, MNRAS, 506, 4933, doi: 10.1093/mnras/stab1956
- Anglés-Alcázar, D., Davé, R., Faucher-Giguère, C.-A., Özel, F., & Hopkins, P. F. 2017, MNRAS, 464, 2840, doi: 10.1093/mnras/stw2565
- Astropy Collaboration, Robitaille, T. P., Tollerud, E. J., et al. 2013, A&A, 558, A33, doi: 10.1051/0004-6361/201322068
- Astropy Collaboration, Price-Whelan, A. M., Sipőcz, B. M., et al. 2018, AJ, 156, 123, doi: 10.3847/1538-3881/aabc4f
- Bouwens, R. J., Oesch, P. A., Illingworth, G. D., Ellis, R. S., & Stefanon, M. 2017, ApJ, 843, 129, doi: 10.3847/1538-4357/aa70a4
- Côté, B., Silvia, D. W., O’Shea, B. W., Smith, B., & Wise, J. H. 2018, ApJ, 859, 67, doi: 10.3847/1538-4357/aaebe8f
- Davé, R., Anglés-Alcázar, D., Narayanan, D., et al. 2019, MNRAS, 486, 2827, doi: 10.1093/mnras/stz937
- de Graaff, A., Trayford, J., Franx, M., et al. 2021, arXiv e-prints, arXiv:2110.02235. <https://arxiv.org/abs/2110.02235>
- Duffy, A. R., Mutch, S. J., Poole, G. B., et al. 2017, MNRAS, 470, 3300, doi: 10.1093/mnras/stx1242
- Endsley, R., Behroozi, P., Stark, D. P., et al. 2020, MNRAS, 493, 1178, doi: 10.1093/mnras/staa324
- Fontanot, F., Calabro, A., Talia, M., et al. 2021, MNRAS, 504, 4481, doi: 10.1093/mnras/stab1213
- Genel, S., Vogelsberger, M., Springel, V., et al. 2014, Monthly Notices of the Royal Astronomical Society, 445, 175–200, doi: 10.1093/mnras/stu1654
- Hainline, K. N., Hviding, R. E., Rieke, M., et al. 2020, ApJ, 892, 125, doi: 10.3847/1538-4357/ab7dc3
- Holwerda, B. W., Bridge, J. S., Steele, R. L., et al. 2020, AJ, 160, 154, doi: 10.3847/1538-3881/aba617
- Huang, K.-H., Fall, S. M., Ferguson, H. C., et al. 2017, ApJ, 838, 6, doi: 10.3847/1538-4357/aa62a6
- Illingworth, G. D., Magee, D., Oesch, P. A., et al. 2013, ApJS, 209, 6, doi: 10.1088/0067-0049/209/1/6
- Iyer, K. G., Gawiser, E., Faber, S. M., et al. 2019, The Astrophysical Journal, 879, 116, doi: 10.3847/1538-4357/ab2052
- Kauffmann, O. B., Le Fèvre, O., Ilbert, O., et al. 2020, A&A, 640, A67, doi: 10.1051/0004-6361/202037450
- Kurczynski, P., Gawiser, E., Acquaviva, V., et al. 2016, ApJ, 820, L1, doi: 10.3847/2041-8205/820/1/L1
- Ma, X. 2018, PhD thesis, TAPIR, MC 350-17, California Institute of Technology, Pasadena, CA 91125, USA
- McLure, R. J., Pearce, H. J., Dunlop, J. S., et al. 2013, MNRAS, 428, 1088, doi: 10.1093/mnras/sts092
- Miller, T. B., & van Dokkum, P. 2021, The Astrophysical Journal, 923, 124, doi: 10.3847/1538-4357/ac2b30
- Mowla, L. A., van Dokkum, P., Brammer, G. B., et al. 2019, ApJ, 880, 57, doi: 10.3847/1538-4357/ab290a
- Narayanan, D., Turk, M. J., Robitaille, T., et al. 2021, ApJS, 252, 12, doi: 10.3847/1538-4365/abc487
- Robson, D., & Davé, R. 2021, arXiv e-prints, arXiv:2107.01206. <https://arxiv.org/abs/2107.01206>
- Rodriguez-Gomez, V., Snyder, G. F., Lotz, J. M., et al. 2019, MNRAS, 483, 4140, doi: 10.1093/mnras/sty3345
- Sorba, R., & Sawicki, M. 2018, MNRAS, 476, 1532, doi: 10.1093/mnras/sty186
- Suess, K. A., Kriek, M., Price, S. H., & Barro, G. 2019, ApJ, 877, 103, doi: 10.3847/1538-4357/ab1bda
- Zheng, Y., Dave, R., Wild, V., & Rodríguez Montero, F. 2021, arXiv e-prints, arXiv:2110.01935. <https://arxiv.org/abs/2110.01935>